Original scientific paper

NEW APPROACH TO EXPERIMENTAL DETERMINATION OF ROTATIONAL PIVOT BEHAVIOUR BY PHOTOGRAMMETRIC MEASUREMENT

Kristina Marković, Maja Dundović, Željko Vrcan

Faculty of Engineering, University of Rijeka, Rijeka, Croatia

Abstract. *This paper discusses an innovative approach to experimentally determine the behaviour of rotational pivot behaviour by photogrammetric measurements. The compliant rotational pivot was selected for research as it is a well understood compliant mechanism whose deformations can be calculated analytically or numerically, allowing easy verification of the results. The mechanism was redesigned for monolithic additive manufacturing with the selection of printing directions that have reduced the influence of material anisotropy. Rapid developments in image processing and computer vision have resulted in integration of photogrammetry and digital image correlation into a wide range of applications. The primary contribution of this article is in the custom designed experimental pure bending load testing setup with an additional optical displacement measurement system, which was used to study the behaviour of additively manufactured compliant mechanisms. A high quality, consumer-grade camera was used for image capture, while image processing was performed using ready-made and custom developed MATLAB tools. Also, a redesigned compliant mechanism with sufficient precision for applications in low-cost, single-use compliant precise positioning systems was developed, and it was determined whether the selected experimental method is applicable to the research of monolithic compliant rotational joints. The experimental results obtained using this method have been compared to results obtained using finite element analysis and analytical calculations, and it was shown that the results are in good concordance. Therefore, it was concluded that photogrammetric analysis aided by feature recognition is applicable to the measurement of parasitic shift of compliant mechanisms.*

Key words: *Compliant mechanism, Parasitic shift, Photogrammetry, DIC, Feature detection*

1. INTRODUCTION

The development and availability of innovative technologies present a constant challenge to design engineers to develop new and innovative machine concepts that will keep them competitive and successful in the targeted market. Compliant mechanisms are mechanical assemblies that transmit motion, power or force without friction, wear, and backlash with excellent fatigue resistance. These mechanisms achieve motion in whole or in part through elastic deformation of compliant parts and provide an alternative to sliding and/or rolling designs. Compliant mechanisms are now widely used in daily life [1,2], especially in mechanical engineering, precision mechanics [3], micro and nano systems technology, metrology [4], seismology, semiconductor manufacturing [4], aerospace engineering, astrophysics, automotive industry, machine tools, precision transfer tools [5], (bio)medical applications, as well as household appliances and medical aids [6,7]. The use of compliant mechanisms offers important advantages, such as high accuracy, precision and motion resolution, and no contact during motion, so there is no wear and friction and therefore the mechanism does not heat up. Consequently, no lubrication is required, the mechanism cannot jam, and no maintenance is required, so the mechanism can operate in almost any environment (e.g., radiation exposure, extreme heat or cold, corrosive, dirty or ultra-clean environments). In addition, compliant mechanisms have a reduced part count, which reduces manufacturing and assembly costs [8,9]. In general, their assemblies are simple, compact, and dependable, especially if they consist of a single part when considered monolithic [10].

Previously, high manufacturing costs were the main disadvantage of compliant mechanisms, however, the rapid progress of additive manufacturing technologies has enabled the manufacturing of complex functional products, the manufacturing costs of such mechanisms have been reduced and the manufacturing of complex monolithic and thin-walled variants has become much easier [11]. Given the obvious advantages and ease of application of compliant mechanisms, the need arose to research the mechanisms and consequently the behaviour of innovative materials, especially those that enable monolithic design and additive manufacturing of compliant mechanisms [12–14]. Therefore, it is necessary to research the applicability of new manufacturing technologies for such constructions so that the mechanisms meet the criteria of strength, stiffness, stability, durability, functionality, and ease of manufacturing, leading to a reduction in energy and raw material consumption during manufacturing [15]. Additive technologies use materials with an extensive range of mechanical properties and a wide range of applications, covering their application in compliant mechanisms [16]. Therefore, an investigation of the properties and behaviour of innovative materials used in the development of compliant mechanism models is appropriate.

Rapid developments in the area of image processing and computer vision, marked by a combination of advancements in various algorithms, hardware capabilities, and breakthroughs in machine learning and deep learning, etc., have played a significant role in enhancing the accuracy, efficiency, and versatility of photogrammetric methods, resulting in the integration of photogrammetry into a wide range of scientific and industrial applications. This includes medical image analysis [17,18], mapping [19,20], autonomous vehicles [21], indoor and outdoor monitoring [22–24], robotics [25–27], and much more.

A fundamental goal of photogrammetry and computer vision is to obtain reliable 3D information from 2D images. Multiple computer vision techniques, such as optical flow,

feature tracking and phase correlation, can be employed for displacement measurement [28–30]. Digital image correlation, or DIC, is one of the most important photogrammetric methods in engineering, materials science, and structural analysis applications. It is a contactless optical measurement technique for the analysis of the deformation and motion of surface objects by comparison of digital images.

The basic processing logic of DIC may be summarized as follows: acquisition of the image, selection of a feature subset, followed by the correlation of images and analysis of displacement/deformation etc. In broader words, the movement of small subsets or patterns is tracked within a series of images captured at various stages of deformation or motion. The analysis of the displacement and deformation of these subsets, allows DIC algorithms to determine the strain and deformation characteristics of the object or surface being researched. The main advantage of DIC is that measurements are made without interfering with the movement or deformation and that measurements are made full field, capturing the deformation information across the entire surface of the object. Because of this, DIC is suitable for both small and large displacements and deformations, making it applicable in the deformation analysis of a wide range of materials and structures.

As with all optical methods, photogrammetry requires calibration to achieve accurate results by accounting for camera distortion, lens characteristics, calibration pattern precision, image quality, lighting conditions, etc. Various reliable and efficient methods of calibration have been developed for this purpose [31–33].

The contribution of this article is in the custom-designed experimental pure bending load testing and displacement measurement setup. The setup was then used to study the behaviour of additively manufactured compliant mechanisms under such load conditions. The extended contribution was made through the successful application of a high-quality, consumer-grade camera and lens, while the image processing was performed using ready-made toolboxes and proprietary code developed for MATLAB. The authors are not aware of a similar setup or experimental method being discussed in the available literature at the time of writing this article.2. Problem Statement

The compliant rotational joint was selected for optomechanical measurements as it is a well-understood compliant element that can be used as a building block for more complex mechanisms. Its deformations can be calculated analytically, allowing for easy verification and cross-checking of experimental and finite element method-based results [34]. Furthermore, the mechanism has the advantage that it can be conveniently redesigned for additive manufacturing as the geometry is simple and printer-friendly with no voids or overlaps, allowing selection of printing directions that will reduce the influence of material anisotropy. Photogrammetry covers a range of precise and accurate optical methods applicable to spatial measurements that are widely used due to their non-destructive and contactless nature, making them particularly suitable for applications in compliant mechanisms.

The design arrangement of a monolithic compliant rotational joint as discussed in this paper, obtained by using spring-strips, as shown in Fig. 1, is often referred to as the cross-spring pivot. It is characterised by considerable compliance along the 'in plane' rotational degree of freedom and high stiffness along the secondary degree of freedom.
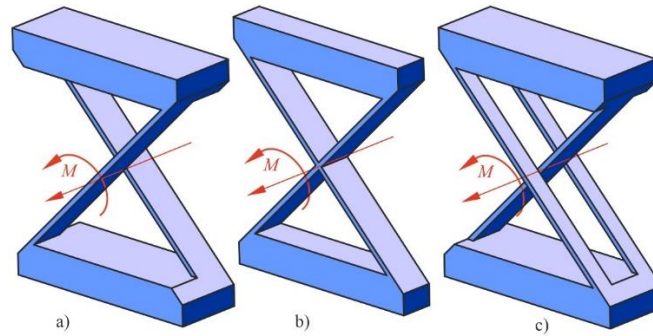
Fig. 1 Rotational cross-spring pivot variants: a) classical two-strip design with strips of equal width; b) conventional monolithic design with intersecting strips; c) three-strip design with equal overall stripe width for both directions

The design of the mechanism as shown in Fig. 1c is the subject of the research performed in this article. This mechanism variant, as shown in Fig. 2a, consists of rigid body B connected by spring-strips 1, 2 and 3, crossing at their midpoints, to block A. In the usual configuration, the used spring-strips have the same length L and thickness t. The width of strips 1 and 3 is equal to one-half of the width of strip 2, $b_1 = b_3 = b_2 /2$. The mechanism, including the spring-strips, was printed monolithically with constant print settings.
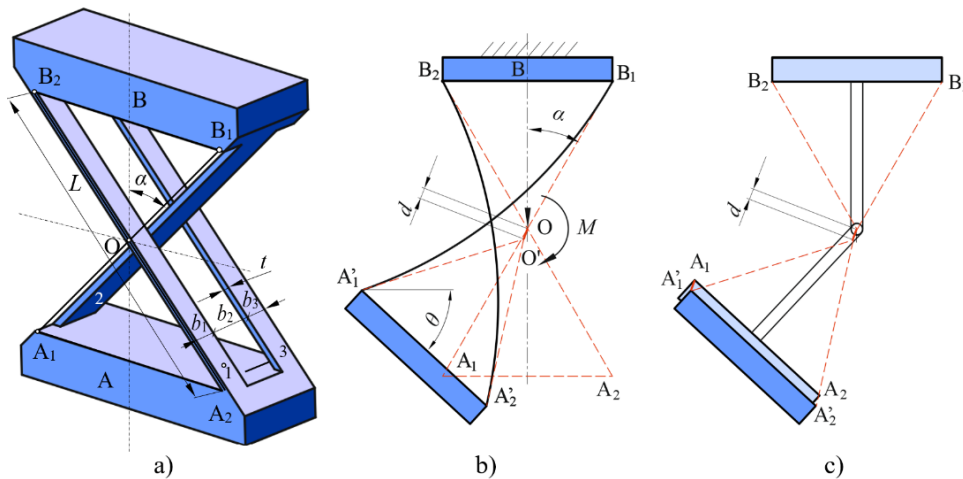

Fig. 2 Three-strip rotational pivot: a) Geometry; b) Parasitic shift; c) Displacement of rigid body A of compliant joint in comparison to conventional rigid joint

In practical use, the rigid bodies A and B experience rotation about each other due to the deflection of the spring-strips (Fig. 2b). In the case of larger rotation angles θ, the 'geometrical' centre of the pivot O moves to point O,' which is defined by the tangents to the fixed ends of the strips on the movable block, resulting in a parasitic shift of amplitude

d and phase φ. The difference between the position of rigid body A (light blue) in the case of a conventional rigid joint and in the case of a compliant joint (dark blue) is shown in Fig. 2c. This parasitic motion is unwanted due to its detrimental influence on the precision of the analysed mechanisms [35,36].

The purpose of the research performed in this article is to develop a redesigned additively manufactured compliant element with sufficient precision to be used, for example, in low-cost, single-use compliant precise positioning systems. Another objective of the research is to determine whether the selected experimental method may be applied to the measurement of parasitic shifts of compliant rotational joints and then extended to compliant mechanisms in general. This will be significant for the analysis of compliant mechanisms whose deformations cannot be calculated analytically.

3. MANUFACTURE OF ROTATIONAL PIVOT

Additive manufacturing processes have become more readily available, and the improved manufacturing processes have resulted in the products advancing from simple dimensional prototypes to usable parts. This has also resulted in the process of additive manufacturing becoming applicable in the production of compliant mechanisms. Monolithic compliant mechanisms, until now, have mostly been machined from solid blocks of metal by complex and expensive manufacturing processes. Additive technologies have made the manufacture of both monolithic and complex geometry-compliant mechanisms readily available.

The compliant mechanism which is the subject of the research in this paper, and its accompanying tensile test samples were manufactured by fused deposition modelling (FDM) using a filament-based process. The tensile test samples and the spring stripes were printed with matched filament laying and load direction. The mechanism was printed on a Prusa MK3S printer using PLA filament. The process parameters are given in Table 1.

Table 1 Printing process parameters

Process parameter	Value
Layer height	0,2 mm
Infill	100%
Filament diameter	1,75 mm
Extruder temperature	215 °C
Bed temperature	60 °C

The mechanism is of the same type and geometry as in [34,35], however, modifications had to be made to accommodate for the constraints of the available additive manufacturing process. The mechanism consists of spring-strips, with the angle between the spring-strips being $2\alpha = 90°$. The spring-strips are $t = 1,5$ mm thick, $L = 115$ mm long, and the respective widths are $b_1 = b_3 = 10$ mm and $b_2 = 20$ mm. The complete mechanism is shown in Fig. 3., with the additions made to the rigid bodies visible in plain sight. The additions are required to connect the mechanism to the testing rig. The purpose of the additions is to minimize the number of parts required to connect the mechanism to the testing rig, and the additions only increase the rigidity of the setup, therefore improving the accuracy of the test results.

Fig. 3 Printed mechanism

4. EXPERIMENTAL SETUP AND PROCEDURES

Two distinct series of experiments were performed, the first being the tensile testing on standard test samples, and the second being the investigation of the compliant mechanism behaviour during rotational deformation with predefined angles of rotation.

4.1 Tensile Testing of Standardized Test Specimens

The tensile tests were performed according to standard ISO 527-2, using universal specimens (Fig. 4) on a STEP Labs electro-mechanical testing machine for static and dynamic testing capable of exerting a maximal static load of 16 kN and a maximal dynamic load of 24 kN. The samples were printed from the same filament spool as the mechanism specimen, using the same printing parameters (Table 1). The test was repeated on five specimens which were loaded at a speed of 1 mm per minute until failure. Young's modulus was determined as the average value of five tensile tests at 110 N/mm^2, and this value was later used for purposes of numerical analysis. The tensile test setup is shown in Fig. 4.

Fig. 4 Tensile testing setup

4.2 Testing of Compliant Mechanism Specimen

The experimental measurements were performed on a testing rig set up on an optomechanical table as displayed in Fig. 5 to determine the parasitic shifts of the geometrical centre of the pivot in the deformed position.
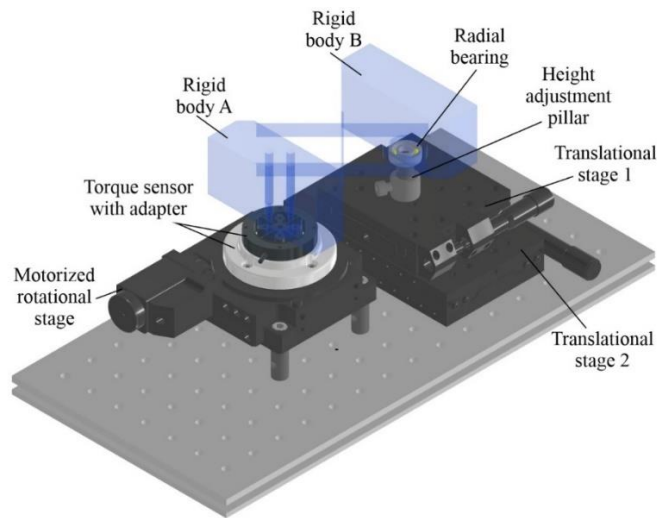

Fig. 5 3D model of the mechanism testing rig

The experimental setup was modularly assembled with consideration to the expected loads and displacements, based on prior experience and basic numeric simulation. Rigid body A of the compliant mechanism is directly bolted onto a motorized rotational stage through a torque sensor, which only allows the rigid body A to rotate around the vertical axis. The motorized rotational stage with an integrated encoder has a resolution of 0,01° and eccentricity of 10 µm or less, while the torque sensor is rated at 0,5 Nm and calibrated to an accuracy of 0,2% of rated torque. The levelling of rigid body B is then performed using a height-adjustable precision pillar with vertical movement of 1 mm per revolution. The combination of a radial bearing and translational stage 1 allows two DOFs to rigid body B. Those two DOFs allow for the parasitic shift to exhibit itself. Otherwise, a constrained rigid body B would result in the parasitic shift placing the mechanism under undue strain. Translational stage 2 is present only to provide proper alignment of rigid bodies A and B. Translational stages 1 and 2 are identical with sensitivity under 1 µm, one inch of travel range (25,4 mm) and an angular deviation under 200 µrad.

The measurements were conducted by rotating rigid body A up to $\theta/2 = 15°$, resulting in body B being rotated for the same angle due to the spring-stripes (Fig. 2b). This gives an overall range of measurement results from $\theta = 0°$ to $\theta = 30°$. The measurement was performed in $\theta/2 = 2,5°$ increments. After each increment, the motorized stage was stopped, a torque reading was made, and a picture was taken. The CANON R5-C camera with RF 100mm F2.8L MACRO IS USM lens was used in the experimental setup. Images for photogrammetric displacement measurements were taken in 8K resolution (45 MP, 8192 x 5464).

The testing rig and measurement system, shown in Fig. 6, were entirely developed in-house for the experimental measurements. MATLAB's Computer Vision Toolbox and Image Processing Toolbox functions were used, more precisely feature detection and extraction, followed by feature matching, and finally calculation of geometrical transformations. Camera calibration, as well as communications and control of the hardware, was also performed using MATLAB.
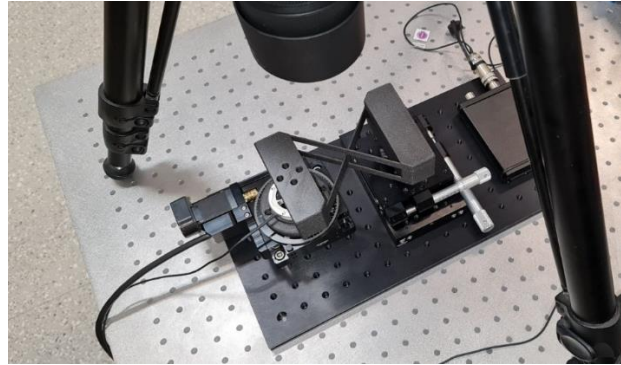

Fig. 6 Experimental setup

Camera calibration must be performed before measurements. The Camera Calibrator application, a part of the MATLAB Computer Vision Toolbox is used for this purpose. It is considered dependable as it accounts for pattern errors and optical errors. The algorithms used by the application are based on the Zhang calibration method [32,33].

A checkerboard pattern of 7x10 squares with a size of 5.08 mm (2/10 inch) was used for the calibration, as shown in Fig. 7. The pattern was adjusted in size for the resolution of the high-quality laser printer used to print the pattern, as well as for the size of the area of the measurement.
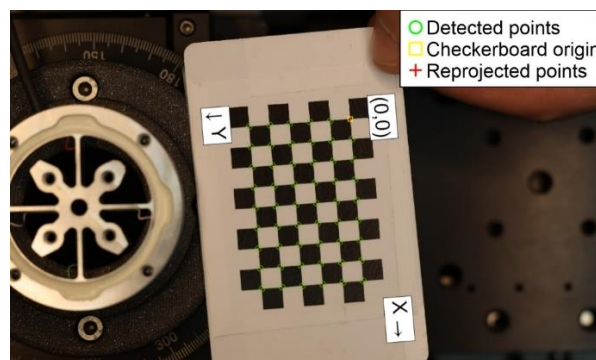

Fig. 7 Checkerboard pattern used for calibration

Calibration is performed with the camera held stationary with the calibration pattern being moved by hand. Eleven images are then captured to complete the calibration process.

The camera settings (focus, aperture, and exposure) from the calibration procedure are then maintained throughout the measurement process. The mean reprojection error was established to be 0,53 pixels or 7 µm, Fig 8.
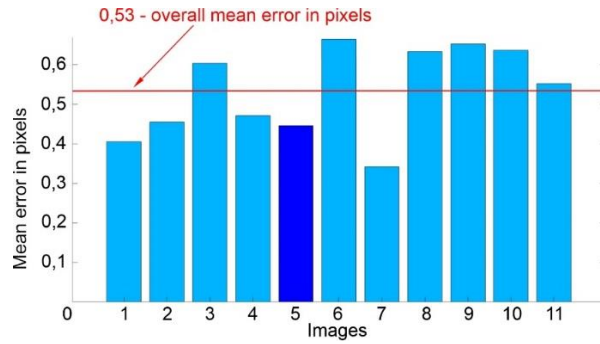

Fig. 8 Mean reprojection error per image

For verification, an additional calibration was performed by placing the measurement scale at six separate locations on the observed surface of the rigid bodies of the compliant mechanism, Fig. 9. Three measurements were performed at each position, and the results of eighteen measurements were averaged. Based on the results, the pixel size for subsequent measurements was established at 16 µm, which is in concurrence with the MATLAB calibration.
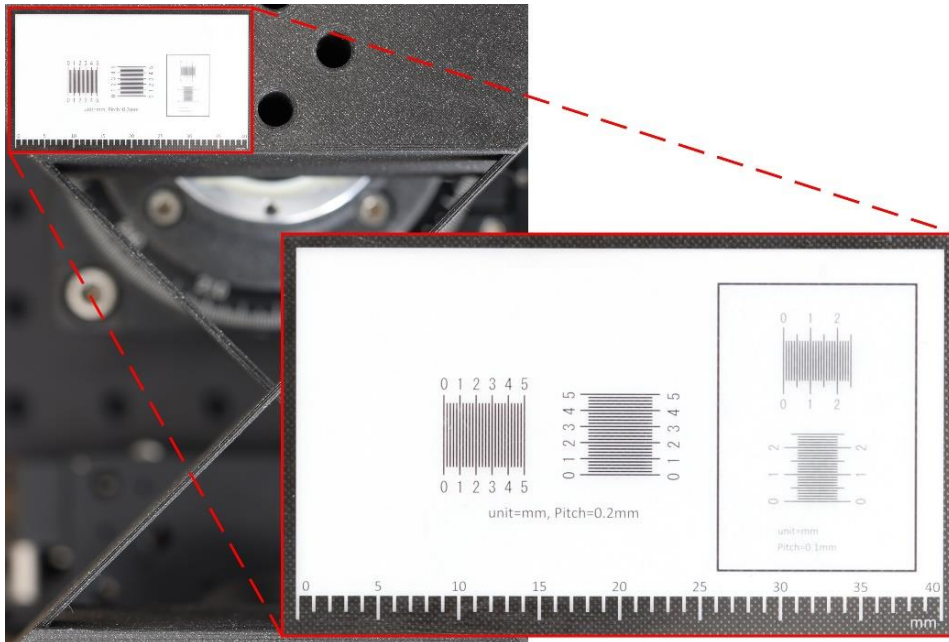

Fig. 9 Feature recognition calibration

Measurements are performed after calibration, and image processing must be performed to extract results. In this case, the features are glitter particles which were built into the test sample during the printing process. Therefore, conventional DIC-based sample preparation (spraying) was not required as the mechanism was printed from a dark-coloured material containing glitter particles. This has also improved the precision and repeatability of the tests as the recognition pattern is built into the sample surface.

The MATLAB functions for feature recognition and extraction utilize the Speeded-up Robust Features (SURF) algorithm, which analyses the initial image and detects the which are then recognized in every subsequent image. The SURF algorithm was chosen because the local features are identified in a way that is invariant to scale, rotation, and illumination changes [37,38].

The displacements were calculated using functions for geometric transformations derived by comparing the locations of matched point pairs from sequential images. The basic principle is shown in Fig. 10, where the software has detected a sequence of geometric transformations, the results of which are marked by yellow lines between the starting locations of the features marked with red circles and the end location of the respective features marked with green crosses.
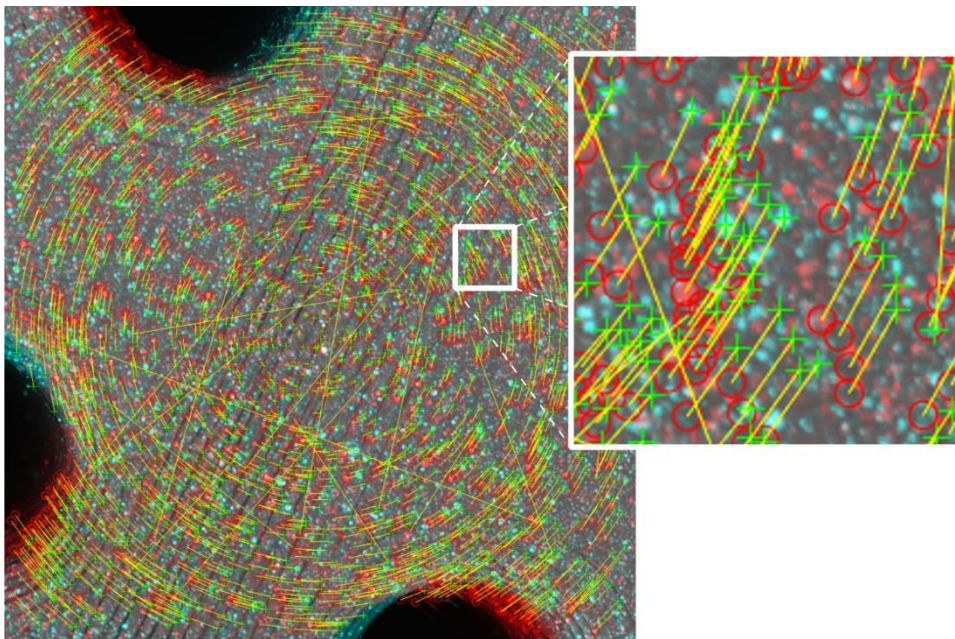

Fig. 10 Measurement procedure

The methodology used is shown in Fig. 11. The axes of the image are labelled in pixels. The software is first tasked with finding the point in the green square on the right that experiences the least amount of movement. This point has been detected and marked with a single red cross. This point has zero translation, and it is coincident with the centre of the rotation imparted by the motorized stage. Then, the green square on the left is searched for the point with the least amount of movement. This point is marked by the blue cross. This

marks the point which is placed exactly above the radial bearing. That point experiences only linear and rotational movement due to the 2 DOF constraint provided by the translational stage and the radial bearing. It has been already mentioned that the linear movement of the translational stage due to the rotation of the compliant mechanism may be used as high-precision displacement.
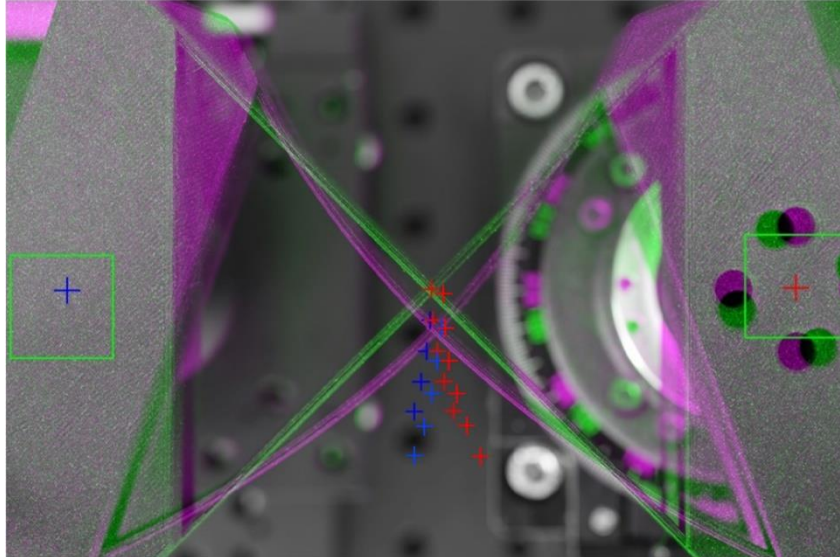

Fig. 11 Feature detection sample image

The sequential red crosses in the centre of the image mark the rotational movement of the joint centre (point O on Fig. 2b) as in the ideal case of a traditional rigid joint, under the assumption that rotation is imparted at the red cross in the green square on the right, while the blue crosses in the centre mark the rotational movement of the joint centre (point O' on Fig. 2b) as in the ideal case of a traditional rigid joint, under the assumption that rotation and appropriate translation is imparted at the blue cross in the green square on the left. The parasitic shift is then measured as the difference between matched blue and red crosses in the centre of the image. The measurements were performed in six incremental steps ($\theta/2 = 2{,}5°, 5°, 7.5°, 10°, 12{,}5°, 15°$).

5. NUMERICAL MODEL

The experimentally obtained results were used to validate the results of the developed numerical model. Numerical analysis was performed using the previously determined value of Young's modulus $E = 110$ N/mm^2, and Poisson's ratio of $v = 0{,}42$.

As it is commonly accepted in the analysis of the behaviour of cross-spring pivots for high-precision applications that it must involve the modelling of large (geometrically nonlinear) deflections of the spring-strips while also including the parasitic shifts of their geometrical centre, that principle was also followed in this case [34,35,39]. Finite element

analysis (FEM) was used for numerical modelling of the kinematics of the cross-spring pivot using non-linear large deflection FEM analysis, using 3-D, 10-node elements having three degrees of freedom at each node.

The constraints of the numerical model were set up to replicate the pure bending case of the experimental setup. The first constraint was placed with the z-axis coincident with the rotational stage rotation axis, allowing only rotation around the z-axis. The second constraint was placed with its z-axis coincident with the axis of rotation of the radial bearing. This constraint allows only rotation around the z-axis, and movement along the longitudinal axis of the mechanism.

The rigid body A was rotated by the aforementioned angles of θ/2 in order to introduce the required loads. The rotation imposed on rigid body A was added in ten equal sub-steps. A stable solution was then iteratively pursued for each sub-step until the convergence criteria were satisfied with fifty iterations allowed for each sub-step. An example of FEM analysis can be seen in Fig. 12, showing the 3D model of the mechanism in the position θ = 30°, overlaid with the wireframe in the unloaded position. The colour scale shows the overall displacement of the points. It was concluded that the overall displacements are in good concordance with the experimental data.
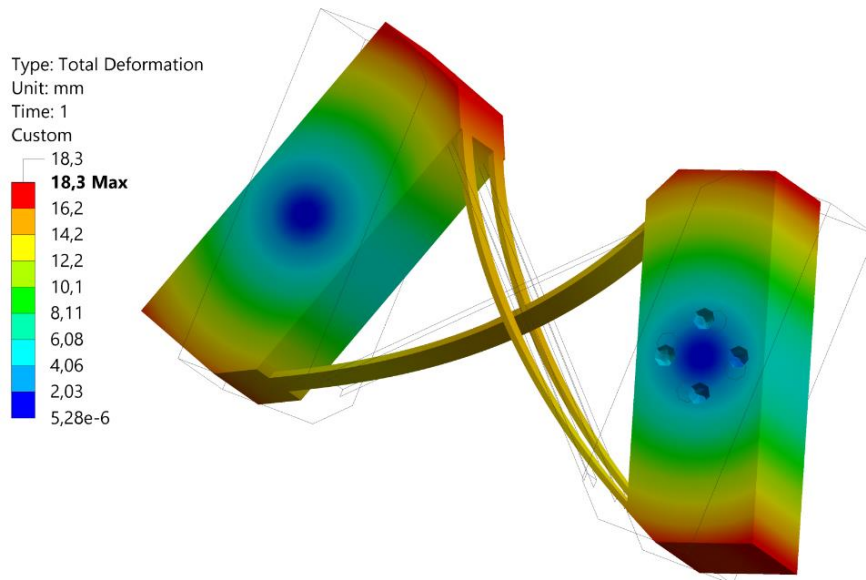

Fig. 12 Results of FEA displacement analysis

6. RESULTS AND DISCUSSION

The results of the experimental measurements were compared with the results of numerical analysis and analytically calculated results [39] (Fig. 13).

The experimental measurement results are marked by blue squares, and they have been connected by a thin dashed line to illustrate the trendline of the experimental results. The

FEA parasitic shift results obtained for rotation angles $\theta = 0...30°$ are well matched with both the experimental measurement results and analytical results obtained in prior work. The differences between the values are within 2-5% for small rotation angles and progressively increase with the rotation angle.

The values of the torque acting on the mechanism have been recorded experimentally using the torque sensor as previously mentioned. The experimentally recorded torque had a discrepancy within 8%. This is attributed to unavoidable minor assembly imprecisions and mechanical losses of the radial bearing and translation stage.

The linear movement of the translational stage due to the rotation of the 3D-printed compliant mechanism may be used for high-precision displacement. The order of magnitude of the displacement is around 350 µm with $\theta/2 = 15°$. The correlation of precise linear displacements to the rotational angle of the mechanism may be seen in Fig. 14.
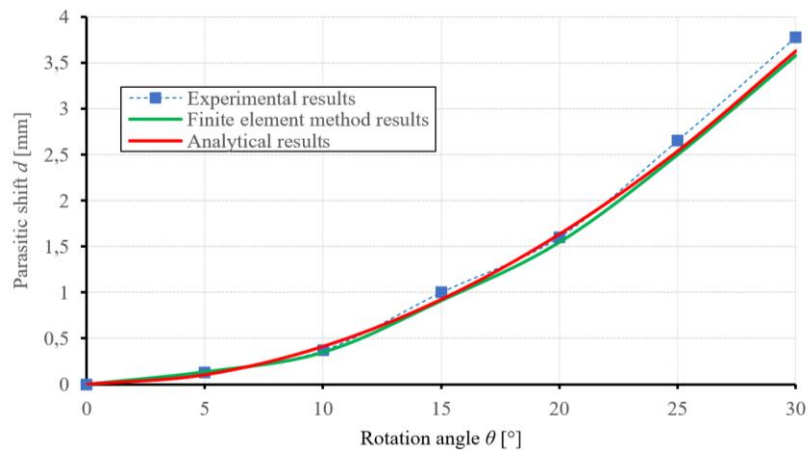

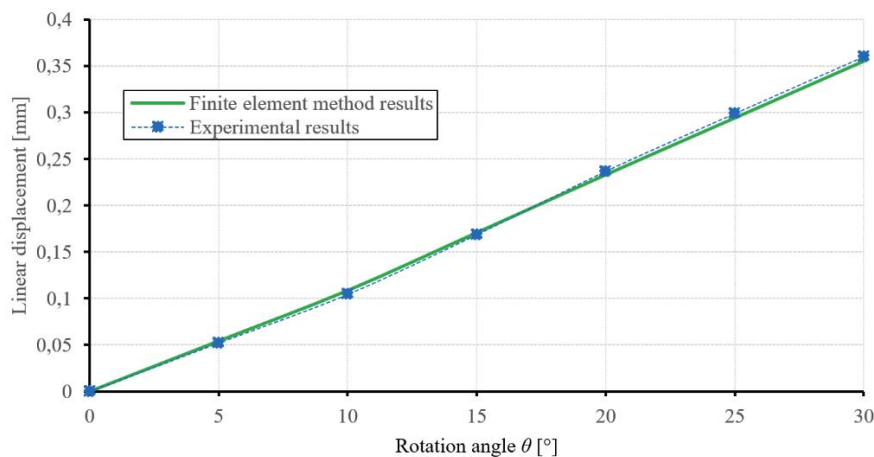**Fig. 13** Comparison of parasitic shift results

Fig. 14 Correlation of precise displacement and rotational angle

The data presented in Fig. 14 shows a correlation between the rotational angle and the linear displacement of the translational stage connected to the rigid body B, and that the correlation is linear, with linearity starting to fall off at rotational angles beyond 30°.

Based on the analysis of the data presented in Figs. 13 and 14, it can be summarized that the selected experimental procedure is applicable to the prediction of the displacement of any point of a compliant element and the behaviour of a custom-compliant mechanism design.

7. CONCLUSION

The measurement of the unwanted parasitic shift of the monolithic rotational compliant mechanism based on spring-stripes using the photogrammetric measurement method aided by SURF feature recognition was covered in this article. To determine the applicability of this method to the measurement of parasitic shifts of compliant mechanisms, the experimental results obtained using this method have been compared to results obtained using finite element analysis.

The test samples and the monolithic mechanism were printed with the same process parameters to keep the material properties consistent. A universal testing machine was used to verify the material properties on standardised test samples.

An appropriate testing setup was developed to properly constrain the mechanism to the required translational and rotational motions. The mechanism was deformed to the required rotational angles, and the torque values were recorded. Images of the deformed mechanism were taken, and photogrammetric analysis was performed to measure the parasitic shift.

The numerical analysis was performed using Young's modulus data gathered by tensile testing of the material samples.

The comparison of the results has shown that the testing results are in accordance with both the FEA and analytically calculated values, with the parasitic shift values within 5%. The discrepancy of the torque values is a bit higher, but still under 8%, and this can be attributed to small imperfections in the testing setup assembly and internal resistances of the radial bearing and translational stage.

During the research into the parasitic shift, it was noticed that the linear movement of the translational stage due to the rotation of the 3D printed compliant mechanism may be used for high precision displacement, as data analysis has shown that a correlation exists between the rotational angle and the linear displacement of the translational stage connected to the rigid body B. This correlation was found to be almost linear, with linearity falling off at increased rotational angles.

Therefore, it was concluded that the results are in accordance and that the method of photogrammetric analysis aided by feature recognition is applicable to the measurement of parasitic shift of compliant mechanisms and monitoring of the behaviour of compliant mechanisms under load.

REFERENCES

1. Jensen, B.D., Howell, L.L., 2002, *The modeling of cross-axis flexural pivots*, Mechanism and Machine Theory, 37(5), pp. 461–476.
2. Choi, Y.-j., Sreenivasan, S. V., Choi, B.J., 2008, *Kinematic design of large displacement precision XY positioning stage by using cross strip flexure joints and over-constrained mechanism*, Mechanism and Machine Theory, 43(6), pp. 724–737.
3. Liu, L., Bi, S., Yang, Q., Wang, Y., 2014, *Design and experiment of generalized triple-cross-spring flexure pivots applied to the ultra-precision instruments*, Review of Scientific Instruments, 85(10), 105102.
4. Dearden, J., Grames, C., Orr, J., Jensen, B.D., Magleby, S.P., Howell, L.L., 2018, *Cylindrical cross-axis flexural pivots*, Precision Engineering, 51, pp. 604–613.
5. Martin, J., Robert, M., 2011, *Novel flexible pivot with large angular range and small center shift to be integrated into a bio-inspired robotic hand*, Journal of Intelligent Material Systems and Structures, 22(13), pp. 1431–1437.
6. Hao, G., Yu, J., Li, H., 2016, *A brief review on nonlinear modeling methods and applications of compliant mechanisms*, Frontiers of Mechanical Engineering, 11(2), pp. 119–128.
7. Schitter, G., Thurner, P.J., Hansma, P.K., 2008, *Design and input-shaping control of a novel scanner for high-speed atomic force microscopy*, Mechatronics, 18(5–6), pp. 282–288.
8. Gonçalves Junior, L.A., Theska, R., Lepikson, H.A., Ribeiro Junior, A.S., Linß, S., Gräser, P., 2020, *Theoretical and experimental investigation of performance characteristics and design aspects of cross-spring pivots*, International Journal of Solids and Structures, 185–186, pp. 240–256.
9. Merriam, E.G., Lund, J.M., Howell, L.L., 2016, *Compound joints: Behavior and benefits of flexure arrays*, Precision Engineering, 45, pp. 79–89.
10. Merriam, E.G., Jones, J.E., Magleby, S.P., Howell, L.L., 2013, *Monolithic 2 DOF fully compliant space pointing mechanism*, Mechanical Sciences, 4(2), pp. 381–390.
11. Khurana, J., Hanks, B., Frecker, M., 2018, *Design for additive manufacturing of cellular compliant mechanism using thermal history feedback*, Proc. Volume 2A: 44th Design Automation Conference, American Society of Mechanical Engineers, IDETC-CIE2018, Quebec City, V02AT03A035.
12. Li, N., Huang, S., Zhang, G., Qin, R., Liu, W., Xiong, H., Shi, G., Blackburn, J., 2019, *Progress in additive manufacturing on new materials: A review*, Journal of Materials Science and Technology, 35(2), pp. 242–269.
13. Baumers, M., Tuck, C., Bourell, D.L., Sreenivasan, R., Hague, R., 2011, *Sustainability of additive manufacturing: Measuring the energy consumption of the laser sintering process*, Proc. Institution of Mechanical Engineers, Part B: Journal of Engineering Manufacture, 225(12), 2228-2239.
14. Banerjee, S., Sutradhar, G., Sahoo, P., 2021, *Design of experiment analysis of elevated temperature wear of Mg-WC nano-composites*, Reports in Mechanical Engineering, 2(1), pp. 202–211.
15. Guo, N., Leu, M.C., 2013, *Additive manufacturing: Technology, applications and research needs*, Frontiers of Mechanical Engineering, 8(3), pp. 215–243.
16. Abaspur Kazerouni, I., Fitzgerald, L., Dooly, G., Toal, D., 2022, *A survey of state-of-the-art on visual SLAM*, Expert Systems with Applications, 205, 117734.
17. Elyan, E., Vuttipittayamongkol, P., Johnston, P., Martin, K., McPherson, K., Moreno-García, C.F., Jayne, C., Sarker, M.M.K., 2022, *Computer vision and machine learning for medical image analysis: recent advances, challenges, and way forward*, Artificial Intelligence Surgery, 2(1), pp. 24–45.
18. Kožar, I., Plovanić, M., Sulovsky,T., 2023, *Derivation matrix in mechanics – data approach*, Engineering Review, 43(1), pp. 1-8.
19. Cheng, J., Zhang, L., Chen, Q., Hu, X., Cai, J., 2022, *A review of visual SLAM methods for autonomous driving vehicles*, Engineering Applications of Artificial Intelligence, 114, 104992.
20. Esteva, A., Chou, K., Yeung, S., Naik, N., Madani, A., Mottaghi, A., Liu, Y., Topol, E., Dean, J., Socher, R., 2021, *Deep learning-enabled medical computer vision*, NPJ Digital Medicine, 4(1), 5.
21. Yang, B., Yang, S., Zhu, X., Qi, M., Li, H., Lv, Z., Cheng, X., Wang, F., 2023, *Computer vision technology for monitoring of indoor and outdoor environments and HVAC equipment: A Review*, Sensors, 23(13), 6186.
22. Hashimoto, K., 2003, *A review on vision-based control of robot manipulators*, Advanced Robotics, 17(10), pp. 969–991.
23. Shahria, M.T., Sunny, M.S.H., Zarif, M.I.I., Ghommam, J., Ahamed, S.I., Rahman, M.H., 2022, *A comprehensive review of vision-based robotic applications: current state, components, approaches, barriers, and potential solutions*, Robotics, 11(6), 139.
24. Spencer, B.F., Hoskere, V., Narazaki, Y., 2019, *Advances in computer vision-based civil infrastructure inspection and monitoring*, Engineering, 5(2), pp. 199–222.

25. Tian, H., Wang, T., Liu, Y., Qiao, X., Li, Y., 2020, *Computer vision technology in agricultural automation —A review*, Information Processing in Agriculture, 7(1), pp. 1–19.
26. Mohsin Abdulazeez, A., Faizi, S., 2021, *Vision-based mobile robot controllers: A scientific review*, Turkish Journal of Computer and Mathematics Education (TURCOMAT), 12(6), pp. 1563–1580.
27. Ryad, A.K., Atallah, A.M., Zekry, A., 2022, *An accurate partial shading detection and global maximum power point tracking technique based on image processing*, Engineering Review, 42(1), pp. 46-55.
28. Liu, W., Ribeiro, E., 2011, *A survey on image-based continuum-body motion estimation*, Image and Vision Computing, 29(8), pp. 509–523.
29. Özyeşil, O., Voroninski, V., Basri, R., Singer, A., 2017, *A survey of structure from motion*, Acta Numerica, 26, pp. 305–364.
30. Sutton, M.A., 2013, *Computer vision-based, noncontacting deformation measurements in mechanics: A generational transformation*, Applied Mechanics Reviews, 65(5), 050802.
31. Heikkila, J., Silven, O., 1997, *A four-step camera calibration procedure with implicit image correction*, Proc. IEEE Computer Society Conference on Computer Vision and Pattern Recognition, IEEE, CVPR-97, San Juan, PR, pp. 1106-1112.
32. Liu, Y., Lv, Z., Zhang, Q., Zhao, J., Fang, Z., Gao, Z., Su, Y., 2023, *Comparison study of three camera calibration methods considering the calibration board quality and 3D measurement accuracy*, Experimental Mechanics, 63(2), pp. 289–307.
33. Percoco, G., Guerra, M.G., Sanchez Salmeron, A.J., Galantucci, L.M., 2017, *Experimental investigation on camera calibration for 3D photogrammetric scanning of micro-features for micrometric resolution*, International Journal of Advanced Manufacturing Technology, 91(9–12), pp. 2935–2947.
34. Marković, K., 2015, *Analysis of Influencing Parameters in the Design of Cross-Spring Pivots*, PhD Thesis, University of Rijeka, Croatia, 183 p.
35. Zelenika, S., De Bona, F., 2002, *Analytical and experimental characterisation of high-precision flexural pivots subjected to lateral loads*, Precision Engineering, 26(4), pp. 381–388.
36. Haringx, J.A., 1949, *The cross-spring pivot as a constructional element*, Flow, Turbulence and Combustion, 1(1), pp. 313–332.
37. Kucak, R.A., Yakar, İ., Bilgi, S., Erol, S., Dervisoglu, A., 2020, *A comparative analysis of speeded up robust features (SURF) and Harris algorithms in point cloud generation*, Intercontinental Geoinformation Days, 1, pp. 5–8.
38. Zhu, S., Ma, W., Yao, J., 2022, *Global and local geometric constrained feature matching for high resolution remote sensing images*, Computers and Electrical Engineering, 103,108337.
39. Marković, K., Zelenika, S., 2017, *Optimized cross-spring pivot configurations with minimized parasitic shifts and stiffness variations investigated via nonlinear FEA*, Mechanics Based Design of Structures and Machines, 45(3), pp. 380–394.